JOURNAL OF AIRCRAFT
Vol. 48, No. 2, March–April 2011

Ducted-Fan Force and Moment Control via Steady and Synthetic Jets

Osgar John Ohanian III* and Etan D. Karni†
AVID LLC, Blacksburg, Virginia 24060
W. Kelly Londenberg‡ and Paul A. Gelhausen§
AVID LLC, Yorktown, Virginia 23692
and
Daniel J. Inman¶
Virginia Polytechnic Institute and State University, Blacksburg, Virginia 24060

DOI: 10.2514/1.C031110

The authors have explored novel applications of synthetic jet actuators for leading- and trailing-edge flow control on ducted-fan vehicles. The synthetic jets on the duct are actuated asymmetrically around the circumference to produce control forces and moments. These forces and moments could be used as flight control effectors for combating wind gusts or reducing control-surface allocation required for trimmed flight. Piezoelectric synthetic jet component design, vehicle integration, and wind-tunnel experimental results are presented with a comparison with steady blowing. The flow control concepts demonstrated production of aerodynamic forces and moments on a ducted fan, although some cases required high-flow-rate steady blowing to create significant responses. The synthetic jets operated at lower blowing momentum coefficients than those used by the steady jets tested. In the duct trailing-edge flow control concept explored, synthetic and steady jets both produced noticeable effects, but from a practical standpoint the ducted-fan application required more flow control authority than the synthetic jets could impart. However, synthetic jets were successful in producing duct leading-edge separation comparable with that obtained from steady jets operating at blowing coefficients that were an order of magnitude higher than those of the synthetic jets.

Nomenclature

A_{disc}	=	fan disc area, $\pi(D^2/4)$
A_{duct}	=	duct planform area, $D \cdot c$
a_j	=	jet orifice area
C_m	=	pitching-moment coefficient, based on fan speed, $M_Y/\rho N^2 D^5$
C_X	=	X force coefficient, based on fan speed, $F_X/\rho N^2 D^4$
C_Z	=	Z force coefficient, based on fan speed, $F_Z/\rho N^2 D^4$
c	=	duct chord
c_s	=	speed of sound
c_μ	=	jet momentum coefficient, $\dot{m}_j U_j/q_{\text{duct}}A_{\text{duct}}$ for steady jets, $n\bar{I}_j/q_{\text{duct}}A_{\text{duct}}$ for synthetic jets
D	=	duct inside diameter (fan diameter)
D_j	=	jet cavity diameter
F_X	=	force in body-fixed X direction
F_Z	=	force in body-fixed Z direction
f	=	synthetic jet drive frequency
f_H	=	Helmholtz frequency
H_j	=	jet cavity depth
h_j	=	jet orifice depth
$\bar{I}_j$	=	time-averaged momentum during outstroke, $\frac{1}{\tau}\rho l_j w_j \int_0^\tau u_j^2(t)\,\mathrm{d}t$
L	=	nondimensional jet slug length, L_0/w
L_0	=	jet slug length, $U_0 T$
l_j	=	jet orifice slot length
M_Y	=	pitching moment about body-fixed y axis
$\dot{m}_j$	=	steady jet mass flow rate
n	=	number of jet slots
N	=	rotational speed of fan in revolutions per second
q_{duct}	=	dynamic pressure inside duct due to induced velocity
q_∞	=	freestream dynamic pressure
Re_{U_0}	=	synthetic jet Reynolds number, $\frac{U_0 w_j}{\nu}$
T	=	thrust
T_{jet}	=	period of jet cycle
U_j	=	spatially averaged steady jet velocity
U_{Peak}	=	phase-averaged peak centerline jet velocity
U_0	=	time-averaged jet velocity over cycle, $\frac{1}{T}\int_0^{T/2} u_j(t)\,\mathrm{d}t$
u_j	=	centerline jet velocity
V_{induced}	=	velocity induced by fan
V_R	=	velocity ratio, U_0/V_∞
V_∞	=	freestream velocity
ν	=	kinematic viscosity
w_j	=	jet orifice slot width
α	=	angle of attack
ΔC_m	=	incremental pitching-moment coefficient due to jet actuation
ΔC_X	=	Incremental X force coefficient due to jet actuation
ΔC_Z	=	Incremental Z force coefficient due to jet actuation
ρ	=	air density
τ	=	jet outstroke time, $T/2$

Presented as Paper 2009-3622 at the 27th AIAA Applied Aerodynamics Conference, San Antonio, TX, 22–25 June 2009; received 21 May 2010; revision received 16 November 2010; accepted for publication 17 November 2010.

*Senior Aircraft Design Engineer; Ph.D. Student, Mechanical Engineering, Virginia Polytechnic Institute and State University, Blacksburg, VA. Member AIAA.
†Aerospace Engineer. Member AIAA.
‡Senior Aircraft Design Analyst. Senior Member AIAA.
§Chief Technical Officer. Senior Member AIAA.
¶George R. Goodson Professor, Mechanical Engineering. Fellow AIAA.

I. Introduction

SYNTHETIC-JET actuators (SJAs) have generated considerable research interest, since they are wider and entrain more flow than similar steady jets [1] and also can be used in situations where steady flow control is not feasible [2]. One such application is active flow control in unmanned air vehicles (UAVs). Depending on the scale of such aircraft, there may not be available volume or weight/power

budget to implement a traditional flow control scheme. The advent of zero-net-mass-flux actuators (another name for SJAs) has theoretically eliminated this hurdle; however, many technical issues must be overcome to successfully implement a system that can meet the performance requirements as well as size, weight, and power constraints of a UAV. This paper develops the use of steady and synthetic jets on a ducted-fan vehicle to create forces and moments for flight control and experimentally verifies the results. The sections that follow cover the synthetic jet component design, vehicle integration, and experimental results from wind-tunnel and static tests, including a comparison with steady blowing.

II. Background, Previous Work, and Innovations

A. Ducted-Fan Background

Interest in ducted-fan vehicles has grown in recent years as the UAV market has expanded and the unique advantages of this configuration are uniquely suited for certain missions. Ducted-fan UAVs take off vertically, can hover, and tilt into the wind for high-speed flight in any direction. Compared with a fixed-wing UAV, the efficient hover capability is a key distinction, whereas the vertical takeoff and landing reduces the logistics footprint for launch and recovery. For the same gross weight, a ducted fan will have a smaller rotor diameter and form factor than those of an equivalent helicopter, the potential for higher top speed, and the added safety of an enclosed rotor. One example of a ducted-fan UAV is the Honeywell RQ-16 T-Hawk [3] (shown in Fig. 1), which has been deployed for military operations in Iraq.

Also known as a shrouded propeller, a ducted fan produces more thrust than a fan (propeller) of the same diameter in isolation [4]. This is due to the thrust/lift produced by the duct lip and the reduction of tip losses. In general, the pressures on the duct surface created by the flow induced by the fan are a large contribution to the overall forces and moments on the ducted-fan unit. In particular, the high-speed flow into the duct induced by the fan causes a low-pressure region on the lip. This phenomenon results in a net force in the thrust direction during hover and can produce lift and pitching moments in forward flight [5], where the duct axis is inclined relative to the freestream. Under certain conditions the flow over the duct lip can separate, affecting the thrust, lift, and pitching moments. It is a complex problem that depends on lip geometry, angle of attack, freestream velocity, and fan rpm [6,7]. In general, ducted fans experience large nose-up pitching moments during transition from hover to cruise (low-speed flight at high angle of attack). The objective of the concepts investigated is to reduce the pitching moment of the vehicle under these conditions in a controlled manner. This reduction in pitching moment would reduce the amount of control vane deflection required to trim during transition to forward flight. For fixed control vane throw, additional vane travel would thereby be made available to maneuver or combat wind gusts.

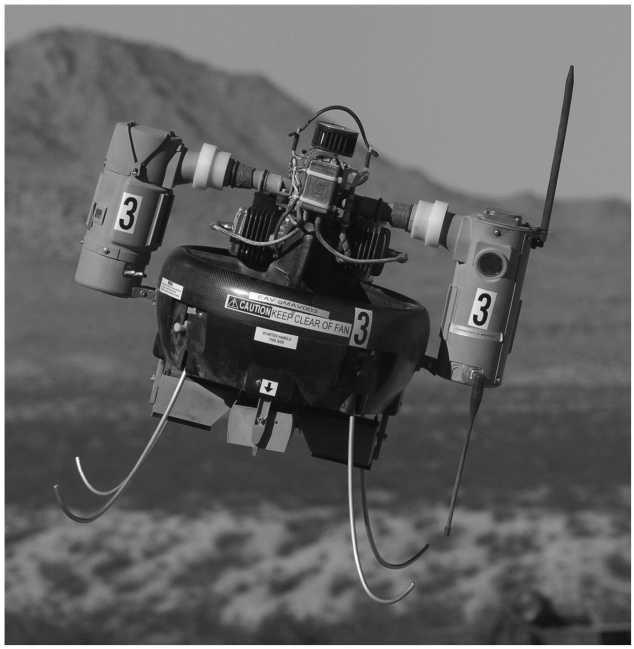

Fig. 1 Example ducted-fan unmanned air vehicle, Honeywell RQ-16 T-Hawk (photo credit to U.S. Navy).

B. Literature Review

NASA put forth significant research effort into ducted-fan configurations in the 1960s. The challenging aerodynamic phenomena of the ducted fan precluded it from wider use as a vehicle configuration at that time. With the advent of more advanced control systems in recent years, many of the challenges of ducted-fan vehicles can now be overcome. The compact form factor, ability to hover, and growth of the unmanned air vehicle market have caused a resurgence of interest in ducted-fan vehicles. The literature pertinent to the subject of this paper can be divided into several categories: fundamental ducted-fan aerodynamics, ducted-fan flow control, and synthetic jet flow control.

1. Fundamental Ducted-Fan Aerodynamics

Yaggy and Mort [8] and Yaggy and Goodson [9] investigated wing-tip mounted ducted-fan aerodynamics. They were some of the first to note the nose-up pitching-moment challenges of the configuration and explored control vane concepts to counteract the effect. Grunwald and Goodson [10,11] explored how the loads on the fan and duct contributed to the overall aerodynamics of the configuration. They confirmed that the duct is the main source of normal force and pitching moment at angle of attack. They also verified the fact that in hover roughly half of the thrust is provided by the duct, and in forward flight at angle of attack the duct carries even more of the load. Mort and Yaggy [12] started looking at ducted-fan aerodynamics from a tip-speed-based nondimensional approach and identified duct stall by observing a change in $dC_m/d\alpha$. Mort and Gamse [13] presented one of the most comprehensive accountings of ducted-fan aerodynamics.

Black et al. [14] gave an extensive look at the effect of the duct in axial flight and pointed out many advantages. They noted that although momentum theory suggests that the stream tube should not contract aft of the duct trailing edge, experiments showed that the pressure was slightly higher than ambient at the duct exit. More recent additions include Martin and Tung [15], who investigated the ducted-fan flowfield, with emphasis on tip-gap and duct-shape effects. Graf et al. [6,16] focused on how the duct lip geometry affects the pitching-moment characteristics in forward flight and how the center of pressure moves over the flight regime. Thipyopas et al. [17] tested a coaxial rotor configuration of ducted fan, investigating blade pitch difference effects on thrust and torque cancellation. Akturk et al. [18] used particle image velocimetry (PIV) to investigate the flowfield through the duct. Pereira [19] gave a comprehensive survey of ducted-fan research and presented results for hover and wind-tunnel tests, comparing open rotors with shrouded rotors.

2. Ducted-Fan Flow Control

Because of the unique aerodynamics of the ducted-fan configuration several researchers have investigated ways to improve or control the flow through the duct. Burley and Hwang [20] showed that tangential blowing of vertical short-takeoff-and-landing engine inlets and diffusers could delay flow separation to higher angles of attack using high-velocity-ratio steady blowing. Kondor et al. [21–23] investigated steady blowing at the trailing edge of the duct to create control forces or augment static thrust. Fung and Amitay [24] used synthetic jets on the stator blades of a cyclic pitch ducted fan to control the yaw angle of the vehicle. Fleming et al. [5,25] explored numerous ways to affect the flow through the duct and over the leading and trailing edges, including vanes, deflectors, thrust reversers, fences, and trailing-edge flaps. They also documented the

equation for calculating the magnitude of momentum drag. Ohanian et al. [26] explored leading-edge and trailing-edge flow control using synthetic jets and compared performance with steady blowing for forward-flight pitching-moment modulation.

3. *Synthetic Jet Flow Control*

Many researchers have investigated synthetic jet design and flow control applications, looking for opportunities to leverage the small form factor of SJAs while enabling new flow control benefits. As research interest began to build in the 1990s, Smith and Glezer [27] addressed many of the fundamental characteristics of jet formation and evolution. Glezer and Amitay [28] reviewed much of the early research that documented jet behavior and applications. Smith and Swift [1] presented an important comparison between synthetic and steady jets, showing that synthetic jets are typically wider and slower than a self-similar continuous jet, but they did not quantify how these attributes affect performance in flow control applications. Holman et al. [29] presented a nondimensional approach concerning jet-formation criteria. Zhong et al. [30] presented an extensive investigation into the fluid mechanics of synthetic jet formation, categorizing the many possible jet structures observed in crossflow according to dimensionless stroke length, velocity ratio, and Strouhal number. Ramasamy et al. [31] presented a detailed investigation into SJA interaction with a crossflow boundary layer using PIV.

Many modeling techniques have been developed for SJAs, including both analytical and numerical approaches. Prominent analytical models include those developed by Gallas et al. [32], Lockerby and Carpenter [33], Sharma [34], and Tang et al. [35]. Numerical approaches using 2-D and 3-D unsteady computational fluid dynamics have been used extensively to study flow inside the cavity and orifice as well as interacting with crossflows [36–40].

Applications of synthetic jet flow control span a diverse range of engineering problems. Amitay et al. [41] studied the use of synthetic jets in engine-inlet-duct separated flow control. Another application of synthetic jets is airfoil separation control; Gilarranz et al. [42] gave an example of increased stall angle of attack and a corresponding increase in maximum lift coefficient. Ciuryla et al. [43] explored flight control of a civil manned aircraft. Farnsworth et al. [44] presented synthetic jet flow control on a UAV from low to high angles of attack. Vukasinovic et al. [45] gave an example of synthetic jet flow control employed in flows over bluff bodies. McMichael et al. [2] developed a novel application of synthetic jets to spinning projectiles, where the frequency of jet actuation was matched to the spin rate, thereby enabling the ability to steer the projectile.

C. Flow Control Concepts

The flow control explored in this paper is uniquely tailored to the ducted-fan flow phenomenon. If the flow over the duct surface can be controlled (i.e., flow turned or accelerated and separation eliminated or produced on demand), then a ducted-fan vehicle could be optimized for combating gusting winds. Asymmetric lift resulting from one side of the duct having attached flow while the opposite side is separated could be used as a control moment or to alleviate undesirable moments due to wind gusts. Achieving attached flow on the entire duct during a typical stall condition could enhance vehicle performance and efficiency. The concepts investigated herein use separation on the leading edge to affect thrust and pitching moment and use a Coandă surface at the trailing edge to create normal force and reduce pitching moment.

In the first concept, the jet is applied against the existing flow over the duct lip, resulting in separation. When the jets are turned off the flow naturally reattaches. This concept is shown in Fig. 2. This separation can decrease the pitching moment experienced during wind gusts and could reduce the amount of flight control actuator usage to maintain stable flight.

In the second concept, the duct trailing edge is replaced by a Coandă surface geometry with a bluff step. When the synthetic jet emanating from the step is turned on, it causes the flow to stay attached to the Coandă surface, thereby causing the primary flow out of the duct to turn. This results in a normal force opposite to the turned flow and a corresponding moment about the vehicle c.g. (typically above the duct trailing edge). When the jet is turned off the flow separates off the bluff corner and the flow travels straight out of the duct. This concept is shown in Fig. 3.

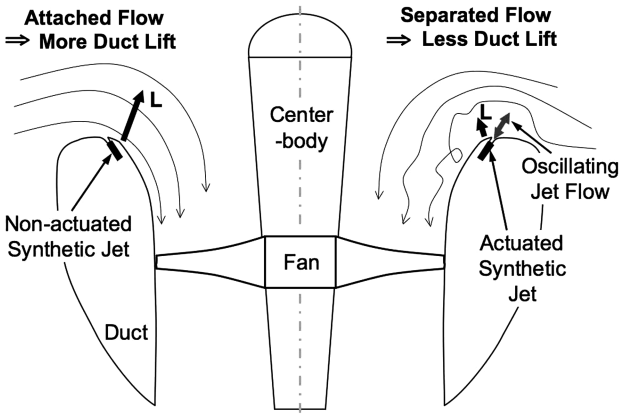

Fig. 2 Duct lip synthetic jet flow control.

A novel use of these two flow control concepts is to apply the control asymmetrically to the duct in order to produce an imbalance in forces, thus resulting in a moment. The net force and moment caused by the asymmetric flow control could be used to control or augment the motion of a ducted-fan vehicle. The target condition for affecting pitching moment on the vehicle design used for this study is trimmed horizontal flight at 35 ft/s freestream velocity with 70 deg angle of attack (20 deg tilt into the wind). This speed represents the critical flight condition of transition between hover and high-speed flight. This flight condition typically requires the most control-surface allocation in the flight envelope, thereby justifying it as a sizing condition for control power.

Steady blowing has been investigated for ducted-fan control forces and moments in hover [21] and to enhance shrouded propeller static thrust [22,23]. This present effort investigates the effects of synthetic and steady jets for hover and for forward-flight conditions over a large range of angles of attack. Other researchers have investigated synthetic jets on the stator blades of a ducted-fan to control vehicle rotation about the propeller axis [24], but controlling the flow over the duct surface here presents a larger opportunity for affecting the overall vehicle aerodynamics. Comparisons between steady and unsteady (synthetic) jets in isolation have been documented [1], but it is the intent of this article to compare steady and unsteady blowing in a specify application of flow control.

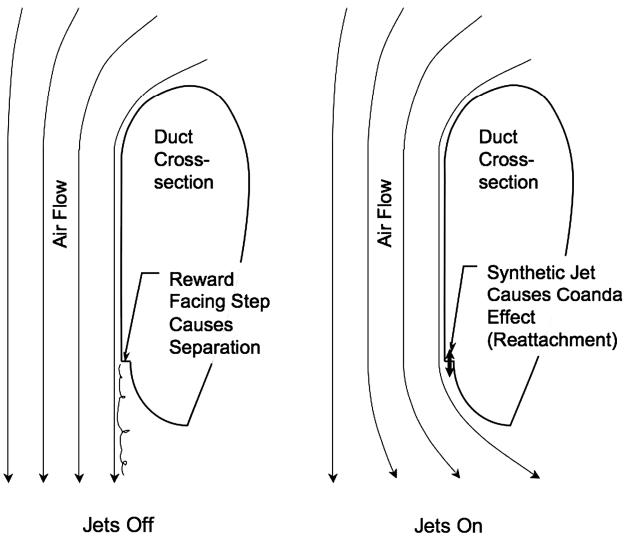

Fig. 3 Duct trailing-edge synthetic jet flow control.

III. Synthetic Jet Component Design

A component development effort was undertaken to design and bench-test synthetic jet actuators based on flight-size piezoelectric elements (27-mm-diam APC FT-27T-3.9A1) to identify anticipated jet velocities for vehicle wind-tunnel testing. The element selected is mass-produced for use as a piezoelectric buzzer and consequently is relatively inexpensive (roughly $1 each). This element has been used by Gomes et al. [46] to produce a peak jet velocity of 420 ft/s (130 m/s) for an 0.05-in.-circular orifice in a normal orientation configuration (jet perpendicular to diaphragm). One of the objectives of this test was to quantify the expected jet velocities for a laterally oriented (jet parallel to diaphragm) rectangular slot with orifice area more than 10 times greater. A long slot orifice is more applicable to the tangential flow control concepts investigated for the ducted-fan application. The bench-test setup is shown in Fig. 4, with a schematic of the cavity layout with the slot-length dimension going into the page.

The input voltage limits used for the piezoelectric diaphragm were ±150 V. Jet velocities were measured with a Dantec 55M01 anemometer with TSI hot-wire probe 1210-T1.5. A hot-wire anemometer can measure velocities at frequencies up to 50 kHz, and it is therefore a favored instrument for measuring SJA flows. The anemometer was calibrated over the range of expected jet velocities (0 to 300 ft/s), and a fourth-order polynomial was used to translate output voltage to air velocity. The hot-wire probe (approximately 0.08-in.-long filament, microns in diameter) was positioned at the center of the slot orifice width and length, one slot width away in the axial direction. Other researchers have recognized this practice as a sufficient method to characterize and compare SJA performance [46]. The hot-wire data were sampled at 40 kHz, the maximum value attainable by the data acquisition system. A dSPACE data acquisition system with Simulink integration was used to run the experiments, automate tests, and collect data. A Trek 50/750 power supply/amplifier was used to generate the high voltages (±150 V) necessary for the piezoelectric elements, but was limited in current to 50 mA. Figure 5 shows the overall setup.

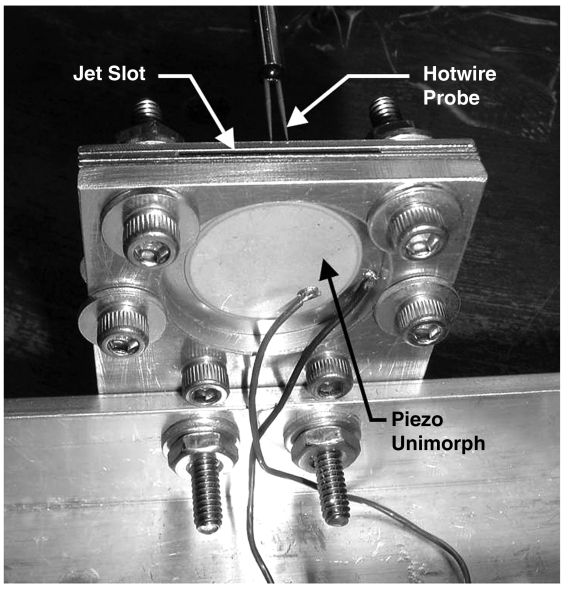

a)

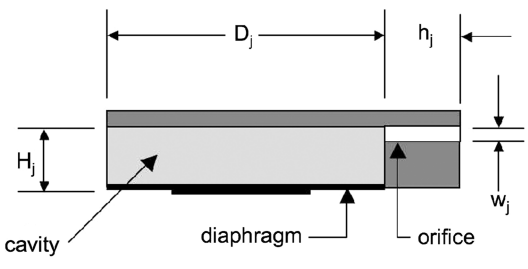

b)

Fig. 4 Synthetic jet arrangement: a) close-up of experimental setup for synthetic jet testing and b) schematic of lateral jet cavity layout.

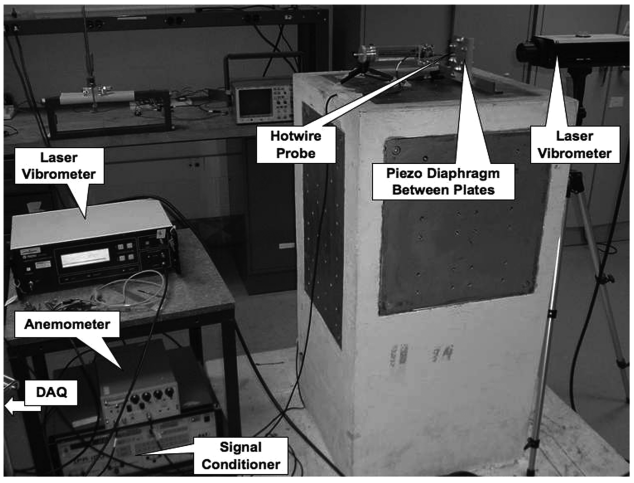

Fig. 5 Synthetic jet bench-test experimental setup.

A. Experimental Results

Synthetic jet output is very dependent on actuation frequency. Two main frequencies dominate their behavior: the Helmholtz frequency of the cavity and the damped natural frequency of the mechanical diaphragm. At the Helmholtz frequency and above, the air in the cavity exhibits compressibility [34]. The relative order of whether the natural frequency of the diaphragm is above or below this frequency dictates what kind of behavior is exhibited. The general finding of this research and other researchers is that the natural frequency of the mechanical diaphragm element is more influential than the Helmholtz frequency in producing the highest jet velocities [46]. Further benefit to jet output can be attained by designing the cavity and diaphragm to align the mechanical natural frequency and Helmholtz resonance frequency [34]. This was not practical for the implementation needed for this flow control application, given the space constraints and chosen diaphragm element. In all of the cases tested the damped natural frequency of the diaphragm was below the Helmholtz frequency of the cavity and produced significantly higher jet output than driving at the Helmholtz frequency. A summary of the cases tested is shown in Table 1, with the corresponding Helmholtz frequency for the specified geometry. The Helmholtz frequency is defined by Eq. (1):

$$f_H = \frac{c_s}{2\pi}\sqrt{\frac{a_j}{h_j V_{\text{cavity}}}} \tag{1}$$

In all cases the diameter of the cavity, D_j, was constant.

After using a sweep of driving frequency to identify the range of the diaphragm damped natural frequency (via a chirp signal), a detailed investigation near the frequency of interest was performed for each configuration. Automated test sweeps were used to collect jet velocity data for a range of frequency, voltage, and driving waveform. This procedure was applied to different configurations of jet geometry including cavity depth and orifice width. Figure 6 shows the results of this process for several cavity depths with constant orifice geometry: a 0.030 × 0.8 in. rectangular slot.

These results show that there is a slight sensitivity in peak jet velocity due to cavity depth. One noticeable difference due to cavity depth is the frequency at which the peak velocity occurs. This frequency is essentially the damped natural frequency of the piezoelectric diaphragm. As the cavity depth and volume increase, the damped natural frequency decreases. This implies greater damping or losses for larger cavities and may imply that shallower cavities are superior. From a space and packaging standpoint, this is a positive

Table 1 Summary of synthetic jet test-case parameters

Orifice Type	D_j, in.	H_j, in.	Volume, in.^{3}	l_j, in.	w_j, in.	h_j, in.	Helmholtz freq., Hz
0.03 × 0.8 in. Slot	1	0.05	0.039	0.8	0.03	0.1	5269
0.03 × 0.8 in. Slot	1	0.06	0.047	0.8	0.03	0.1	4810
0.03 × 0.8 in. Slot	1	0.07	0.055	0.8	0.03	0.1	4453
0.03 × 0.8 in. Slot	1	0.08	0.063	0.8	0.03	0.1	4166
0.02 × 0.8 in. Slot	1	0.06	0.047	0.8	0.02	0.1	3927
0.04 × 0.8 in. Slot	1	0.06	0.047	0.8	0.04	0.1	5554

finding. The peak jet velocity observed from these data is 225 ft/s for a 130-V-amplitude square-wave input at 2400 Hz for a cavity depth of 0.06″.

The effect of orifice slot width was explored while using a constant cavity depth of 0.06 in. The general trend is that the widest slot produced the lowest peak velocities. To take a closer look at this trend, only the highest-voltage square-wave results are superimposed for comparison in Fig. 7.

The widest slot tested, 0.040 in., showed the lowest peak velocity. This makes sense conceptually: for a given volume displacement or mass flow, the velocity is inversely proportional to exit area. If this trend applied indefinitely, the smallest area slot (0.020 in.) would show significant increases over the 0.030 in. slot, but this is not observed. The 0.020 and 0.030 in. slots produce nearly the same peak velocities, although at different frequencies. This is attributed to losses building up as the orifice width decreases and is supported by the decrease in damped natural frequency. This implies that there is an optimal jet width for any synthetic jet design that balances orifice losses with orifice area. If the slot width decreased to values smaller than 0.020 in this case, it is anticipated that the overall jet velocity would decrease due to losses. For this setup the optimum width was ascertained to be in the realm of 0.020 to 0.030 in. For wind-tunnel vehicle testing, the 0.030 in. width slot was selected for two reasons: first, it is easier to fabricate within tolerances; second, it attains roughly the same velocity with a larger area and will therefore impart more momentum to the flow.

The difference in jet performance based on driving-voltage waveform can be observed in Fig. 8. The results show that a square-wave driving function produces roughly a 20% increase in peak jet velocity over a sinusoidal input.

It should be noted that the square wave was the input to the high-voltage amplifier and that only after further investigation measuring the voltage and current entering the piezoelectric diaphragm was it found that the output of the amplifier (which had current limiting protection) was not a clean square-wave form, but more sinusoidal in nature. The square-wave input merely increased the voltage and current amplitude output of the drive circuitry. Driving a capacitive

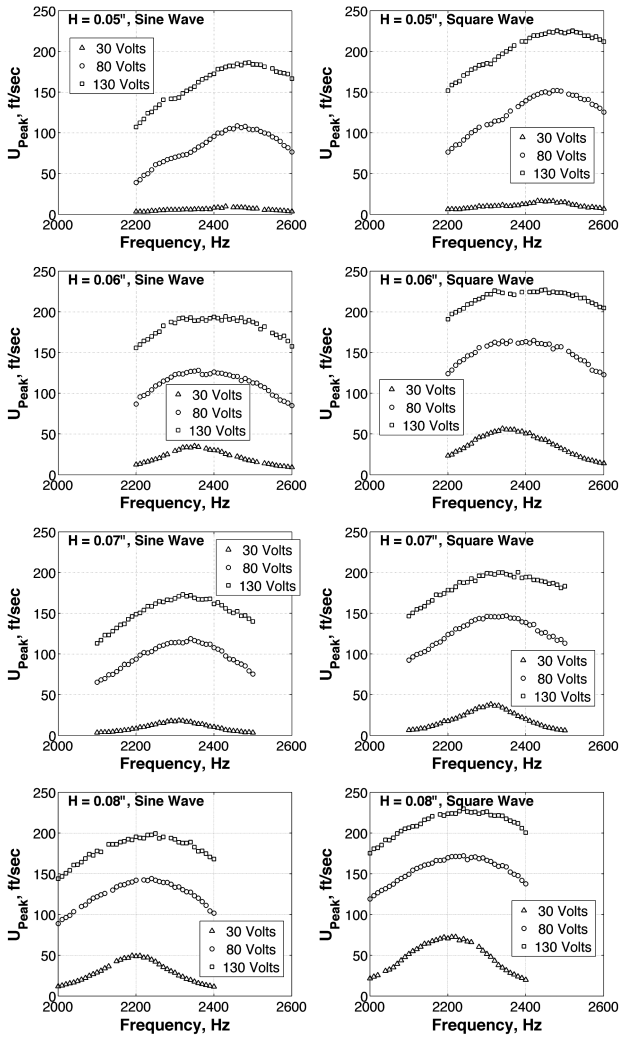

Fig. 6 Frequency, voltage, and waveform sweep for various cavity depths for fixed slot width of 0.03 in.

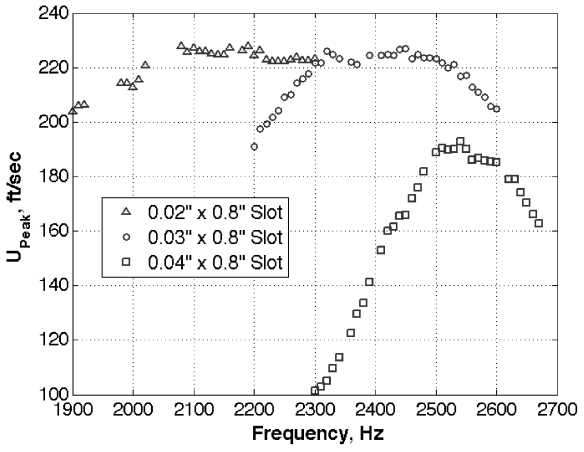

Fig. 7 Effect of orifice width on peak jet velocity characteristics.

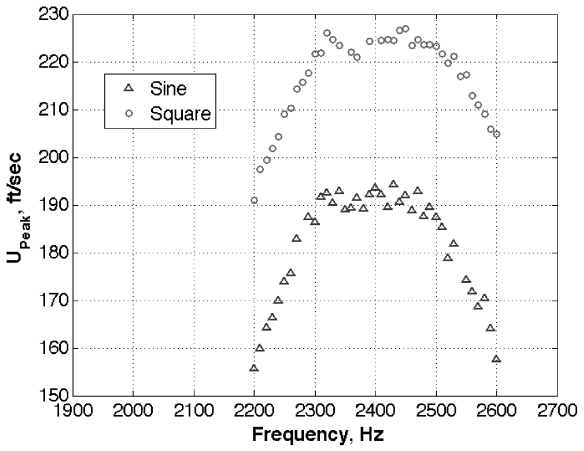

Fig. 8 Effect of driving waveform on peak jet velocity.

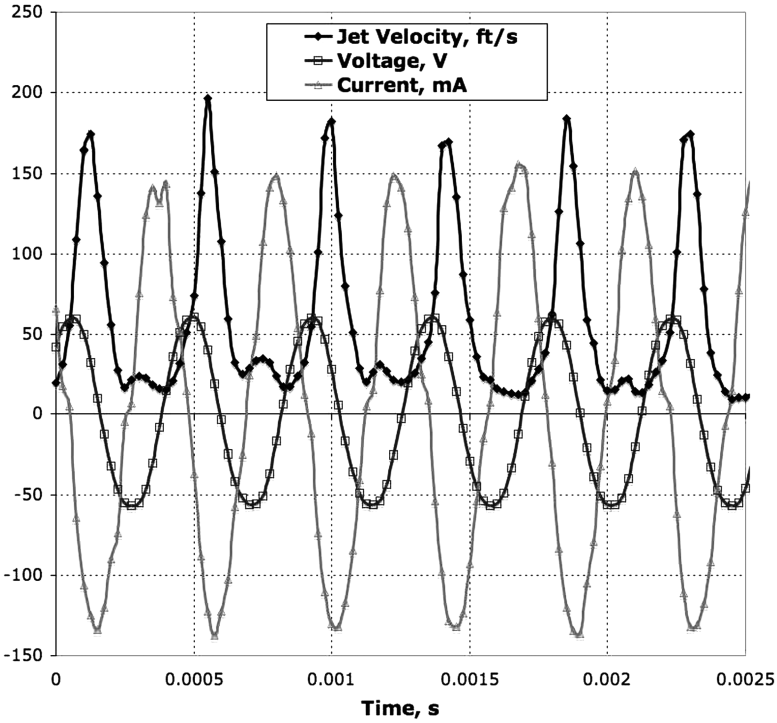

Fig. 9 Jet velocity, input voltage, and input current signals for 2300 Hz sinusoid drive waveform.

piezoelectric diaphragm with a near-square-wave input would result in very large instantaneous currents and large rms current and power draw while driving it at its natural frequency. Square-wave inputs are more wearing on the diaphragm and also tend to excite higher-frequency harmonics, which are not beneficial. The first bending mode of the diaphragm produces the most jet output, due to that mode creating the largest volume displacement. Therefore, sinusoidal waveforms that maximize voltage and current amplitude within the constraints of the drive electronics and durability of the piezoelectric element will result in the highest sustainable jet outputs that do not damage the piezoelectric diaphragm.

Examples of the centerline jet velocity, input voltage, and input current to the synthetic jet are shown in Fig. 9 for a sinusoidal input of 2300 Hz. The voltage and current are roughly 90 deg out of phase, which shows that the mechanical system is near resonance, if a second-order system (mass–spring–damper) approximation is assumed. A negative current corresponds to an outstroke movement of the diaphragm, as the data show the peak jet output roughly in phase with the current.

The parameters of the data set shown in Fig. 9 are representative of those used in the vehicle wind-tunnel tests. The peak jet velocities observed are in the vicinity of 200 ft/s. The small secondary peaks in the troughs of the velocity data are due to the inflow into the slot, measured one slot width downstream. The hot-wire anemometer measures the velocity magnitude, thereby resulting in an absolute value of the actual velocity. Because of the small magnitude and absence of a secondary peak in several periods, rectifying the velocity data was omitted. Integrating the centerline velocity shown over the outstroke time period according to Eq. (2) from Holman et al. [29] results in a time-averaged velocity U_0 of 49.8 ft/s and stroke length L_0 of 0.26 in.:

$$U_0 = fL_0 = \frac{1}{T_j}\int_0^{T_j/2} u_j(t)\,\mathrm{d}t \tag{2}$$

The dimensionless stroke length L_0/w_j for this case is 8.7.

Note that the time-averaged velocity, which is used in flow control application calculations, calculated from the experimental data is roughly one-fourth of the peak jet velocity. This is in fair agreement with the analytical prediction for pure sinusoidal flow velocity in the orifice throat, where average outstroke velocity should be the peak velocity divided by π. The difference observed here may be attributed to measuring the jet velocity one slot width downstream of the orifice instead of directly within the orifice. Since there are practical limits on the maximum peak velocity, this substantial difference from the peak jet velocity makes it more difficult to attain high blowing momentum coefficients using synthetic jets when compared with steady jets.

Using this time-averaged outstroke velocity and adapting the Reynolds number equation from [29] to employ slot width instead of diameter, as shown in Eq. (3), results in a value of 818:

$$Re_{U_0} = \frac{U_0 w_j}{\nu} \tag{3}$$

The inverse of the Strouhal number (a function of Reynolds and Stokes numbers) adapted from [29] to use jet width and Re_{U_0} is depicted in Eq. (4):

$$\frac{1}{Sr} = \frac{(L_0/w_j)}{\pi} = \frac{2U_0}{\omega w_j} = \frac{(2U_0 w_j/\nu)}{(\omega w_j^2/\nu)} = \frac{2Re_{U_0}}{S^2} \tag{4}$$

A value of 2.75 was attained for the data presented and is representative of the jet performance as installed in the vehicle model. This value is well above the jet-formation criterion of 0.16 as predicted by [29].

B. Synthetic Jet Component Design Summary

Peak jet velocities of 200 to 225 ft/s were attained with slot and cavity geometry and orientation similar to the anticipated application. A slot width of 0.030 in. was chosen for going forward into wind-tunnel model design and testing. It was found that shallower cavity depths were desirable from a jet performance standpoint, and this fact also aids in packaging such actuators in a vehicle with limited volume for components.

IV. Synthetic Jet Actuator Vehicle Integration

One of the challenges in developing the wind-tunnel vehicle model was the integration of the piezoelectric diaphragm elements. Three main criteria drove the design of the wind-tunnel model SJA installation. These were as follows:

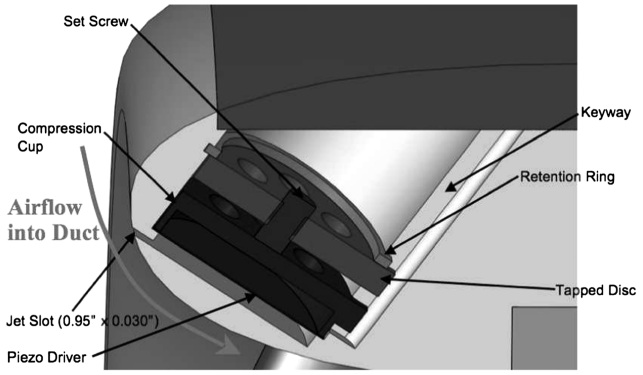

Fig. 10 Piezoelectric diaphragm mounting for leading-edge blowing configuration.

1) Minimize lateral spacing between SJA, to more closely approximate a uniform jet along the entire circumference of the duct.

2) Provide consistent clamping loads for each SJA, to improve boundary condition uniformity.

3) Securely but nonpermanently install the piezoelectric diaphragms in the model. This is necessary to minimize downtime from any diaphragm failures encountered during the wind-tunnel test.

The final concept selected was an axial screw clamp, shown in Fig. 10. Although it requires slightly more parts than other options, it allows for simple replacement of elements, has excellent adjustability, and yields minimum lateral spacing between SJA, thereby increasing the coverage of the duct circumference. For a flight implementation, the piezoelectric elements would be directly bonded into the cavity to minimize volume and weight.

Figure 10 shows how the jet and cavity are oriented in the duct lip, with the outside of the duct toward the top of the figure. The flow would proceed into the duct, and the jet orifice is oriented to oppose this flow at roughly 45 deg. The internal parts of the wind-tunnel model that housed the piezoelectric diaphragms were machined aluminum, with bored holes to hold the elements. A compression cup presses down on the edge of the piezoelectric diaphragm to apply a uniform clamping load. A tapped disc with setscrew is then inserted, with a retention ring finally snapping into place to support the tapped disc. The setscrew is advanced to push on the compression cup and apply the necessary clamp load uniformly to the diaphragm edge. The added benefit of this approach was that a single input (screw torque) was used to tune the boundary condition for the piezoelectric elements. The coverage of the duct lip attained for the leading-edge blowing is 75%.

The trailing-edge geometry shown in Fig. 11 aligns the jet orifice tangential to the Coandă surface to blow in the same direction as the flow through the duct. To minimize the travel from the cavity to the orifice opening the jet cavity is positioned parallel to the duct inside wall (toward the bottom of the figure). The internal features to hold the piezoelectric elements are identical to the leading-edge geometry. The jet coverage attained on the Coandă surface is 85%.

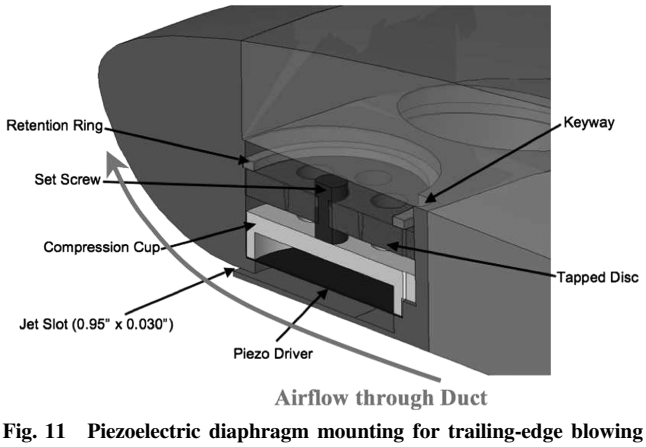

Fig. 11 Piezoelectric diaphragm mounting for trailing-edge blowing configuration.

V. Experimental Setup and Procedure

Static (hover) tests were performed in a high bay area and wind-tunnel tests were performed in the Virginia Polytechnic Institute and State University (Virginia Tech) 6×6 ft Stability Wind Tunnel. The vehicle model was fabricated from machined aluminum and nylon as well as rapid-prototyped resin parts. The base configuration consisted of a duct, 1-ft-diam fan, stator assembly, and fuselage. The model was supported by a six-component force and moment balance in a side-mount orientation to align the most sensitive channel of the balance with the vehicle's pitching-moment axis (y axis). Pitch sweeps were executed by rotating the wind-tunnel turntable on which the balance is mounted. An illustration of the balance and vehicle is shown in Fig. 12, along with the coordinate system used for collecting data. The data presented herein are transformed to move the moment reference center to the center of the duct lip as a simple datum for the vehicle design.

The force and moment balance range and the uncertainty in measured forces and moments at the model reference center are reported in Table 2. The uncertainty in nondimensional variables derived from the test data [listed later in Eqs. (3–5)] is also shown, as calculated using the procedure found in AIAA Standard S-071A-1999 [47]. The primary terms of interest for this analysis are F_X, F_Z, and M_Y. Therefore, the most accurate moment axis of the balance was aligned with the vehicle pitch axis, as can be seen in the table. The uncertainty in turntable angular values (vehicle angle of attack) is estimated at 0.2 deg, as this represents the maximum value observed in daily realignment procedures after many turntable sweeps.

The solid and wake blockage assessed using the principles in Barlow et al. [48] for unusual shapes is 0.59 ft^2 compared with a tunnel cross-sectional area of 36 ft^2. This would result in higher velocities than the nominal tunnel velocity passing around the model, if the model was unpowered. With a powered model, the fan entrains a significant portion of the flow, thus requiring a different correction. The net result is slower flow outside the model, as described in Glauert [49], where he derived corrections for testing propellers in closed wind tunnels. Other approaches include the Hackett et al. [50] and Mikkelsen and Sørensen [51] techniques, but experimental results by Fitzgerald [52] suggest the Glauert correction matched empirical observation best. Although the nondimensional scheme used herein is not affected by the freestream velocity, it is noted that the equivalent airspeed was 0.95 to 0.98 of the nominal tunnel velocity for the range of tests performed.

Figure 13 illustrates this coordinate system along with the angle-of-attack convention, in which the origin is on the fan axis of the vehicle in the plane of the duct lip. All moments are referenced to this

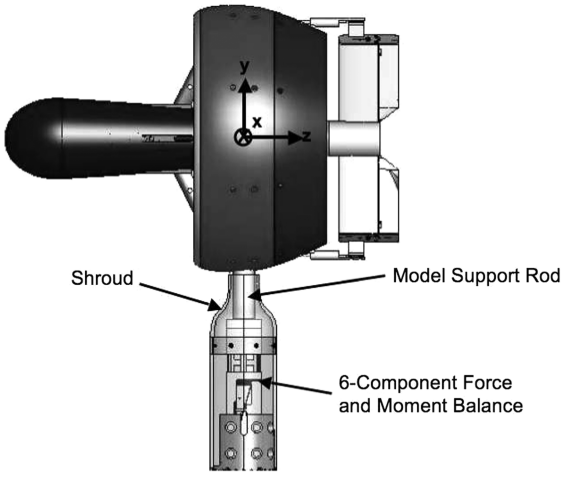

Fig. 12 Balance mounting of wind-tunnel model.

Table 2 Balance range and uncertainty

Term	Balance range	Uncertainty (dimensional)	Uncertainty (nondimensional)
F_X	±120 lb	0.25 lb	0.011
F_Y	±120 lb	0.2 lb	0.008
F_Z	±120 lb	0.25 lb	0.011
M_X	±100 ft-lb	0.4 ft-lb	0.017
M_Y	±30 ft-lb	0.1 ft-lb	0.004
M_Z	±100 ft-lb	0.4 ft-lb	0.017
Shaft power	——	0.08 HP	——

origin. The x axis points out of the duct radially in the preferred flight direction, the y axis points out the right side of the duct, and the z axis points down the fan axis in the same direction as the fan flow. This results in thrust producing a negative force in the z direction and a normal force producing a negative force in the x direction. A nose-up moment relative to the wind corresponds to a positive pitching moment in this coordinate system. The airplane convention for angle of attack is used throughout, where 0 deg represents the nose directly into the wind (also the condition for a pure vertical climb), and 90 deg would vertically orient the vehicle in a pure horizontal wind. Descent would equate to a 180 deg angle of attack, illustrating the large 180 deg angle-of-attack range of such a vehicle.

Multiple configurations of the vehicle model were used to explore the effects of the synthetic jets as well as steady blowing using a compressed-air supply. Synthetic jet velocities in the vehicle slots were measured statically with the hot-wire anemometry, as described in a previous section. The trailing-edge peak velocities were comparable with bench-test results (∼200 ft/s), but leading-edge peak velocities were roughly 60% of the bench-test values. This was attributed to the orifice depth being longer (due to manufacturing constraints) and the increased losses due to this resulted in a lower jet output and damped natural frequency. The optimum drive frequency for trailing-edge actuation was 2300 Hz and for leading-edge actuation was 1900 Hz.

Removing the piezoelectric diaphragms and related mounting hardware and supplying pressurized air to a plenum channel that connected the jet cavities enabled steady blowing with minimal change to the model. Steady velocities were set using a Dwyer inline Visi-float® mass flow meter, with pressure-corrected volumetric flow rates ranging from 15 to 50 ft^3/min. This translated to steady velocities ranging from 160 to 510 ft/s. Hot-wire anemometry was used to verify the flow speed and uniformity between jets. The flexible tubing for supply air was affixed to the rigid shroud outside the balance (as shown in Fig. 12), with slack between the shroud and vehicle model to isolate the force and moment measurements from unintended interference effects. Steady and synthetic jet blowing tare runs with the propeller stopped and wind off did not show significant force and moment response. Only eight of the slots were employed in tests, accounting for one-quarter of the duct circumference.

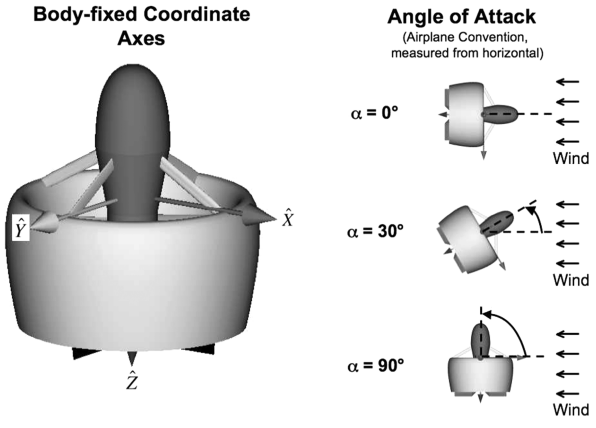

Fig. 13 Body-fixed coordinate system and angle-of-attack convention.

The model was installed in the Virginia Tech Stability Wind Tunnel and is pictured below in Fig. 14. Figure 15 shows the Coandă trailing-edge component installed in the vehicle, with a close-up view of the curved 0.030 in. slot geometry. The leading-edge and trailing-edge flow control components were both machined from aluminum, and electrical-discharge machining was employed to obtain precise slot geometry. The components were anodized to electrically isolate the piezoelectric components from the rest of the model. Figure 16 shows the leading-edge flow control duct lip installed in the vehicle. The airflow over the duct naturally comes from the outside toward the fan. The slots are oriented to point outward, such that when blowing is actuated the flow over the lip could be caused to separate on demand.

VI. Wind-Tunnel and Static Experimental Results

A. Flow Visualization of Flow Control Concepts

In addition to collecting data from the force and moment balance, flow visualization was captured via video. This is helpful in communicating the overall phenomenon that is occurring. One of the most successful concepts was the Coandă trailing-edge blowing at lower flight speeds and high blowing velocities. Two still frames from the video are shown in Fig. 17 for a 35 ft/s freestream flow, with the vehicle tilted 20 deg into the wind (coming from the right in the photograph).

Fig. 14 Vehicle model installed in the Virginia Tech 6 × 6 ft wind tunnel.

Fig. 15 Coandă trailing-edge flow control slot geometry.

Fig. 16 Leading-edge flow control configuration in the wind tunnel.

In the first image, the Coandă blowing is turned off and the tufts on the Coandă surface at the duct exit are fluttering and imply separated flow. The tuft wand in the duct exit flow (stream tube) is being greatly influenced by the freestream flow coming from the right and is bending past the lower centerbody. In the second image, the highest steady rate is in effect and the tufts on the Coandă surface are fully attached. This flow causes the whole stream tube to expand and turn upstream, as can be noted from the large angular change in the tuft wand.

Figure 18 shows similar visualization for the leading-edge concept for a 35 ft/s freestream flow at an angle of attack of 70 deg (tilted 20 deg into the wind).

The leading-edge flow control has the opposite effect of that of the trailing edge: when turned off the lip is fully attached, but when actuated, full flow separation is caused. When the flow is attached, the thrust gained by the suction results in a nose-up pitching moment. When the flow is separated there is a loss of thrust and a decrease in pitching moment. Although a loss of thrust sounds disadvantageous, a crosswind in hover can cause increased lift on the vehicle resulting in an upward acceleration. If the vehicle is trying to maintain a fixed altitude, this ability to cancel the added lift from the crosswind through high-bandwidth actuation is desirable.

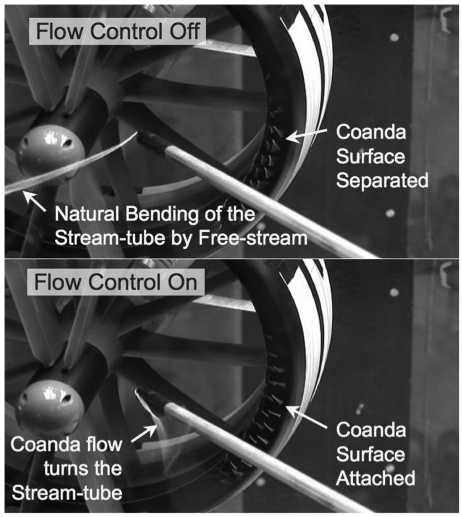

Fig. 17 Photographs of no blowing, separated, Coandă trailing-edge surface, $V_\infty = 35$ ft/s, $\alpha = 70$ deg, and $c_\mu = 0$ (top) and steady blowing, Coandă surface fully attached, $V_\infty = 35$ ft/s, $\alpha = 70$ deg, and $c_\mu = 0.128$ (bottom).

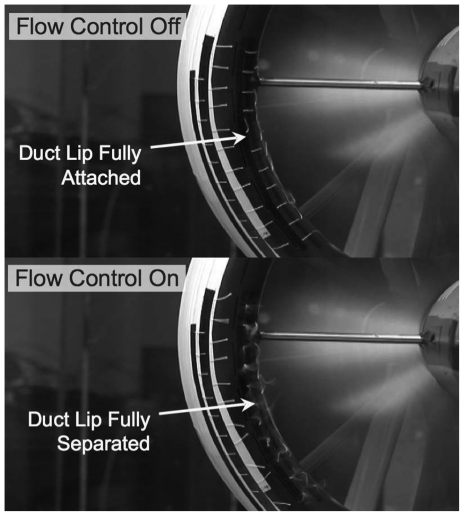

Fig. 18 Photographs of no blowing, attached leading edge, $V_\infty = 35$ ft/s, $\alpha = 70$ deg, and $c_\mu = 0$ (top) and of steady blowing, duct lip fully separated, $V_\infty = 35$ ft/s, $\alpha = 70$ deg, and $c_\mu = 0.101$ (bottom).

In summary, the flow visualization results showed that both flow control concepts achieved their desired intent and can significantly affect the flow. The remaining sections will discuss the specific performance of each of these concepts and how they affect the vehicle forces and moments.

B. Nondimensional Approach for Ducted-Fan Flow Control Data

Ducted-fan vehicles present a unique problem for formulating nondimensional coefficients for blowing momentum and vehicle forces and moments. Because the freestream dynamic pressure used in most approaches goes to zero when the vehicle is hovering, a different approach is needed. An approach that can span hover to forward flight is optimal and therefore must be based on some common parameter to both regimes. The fan tip speed or the flow induced through the duct are possible candidates. For vehicle forces and moments, the form typically used for propeller thrust coefficient will be applied to the normal and axial forces as well as the pitching moment. These are represented in Eqs. (5–7), respectively:

$$C_X = \frac{F_X}{\rho N^2 D^4} \tag{5}$$

$$C_Z = \frac{F_Z}{\rho N^2 D^4} \tag{6}$$

$$C_m = \frac{M_Y}{\rho N^2 D^5} \tag{7}$$

where ρ is the air density, N is the rotational speed of the fan in revolutions per second, and D is the fan diameter. The blowing momentum coefficient typically used for fixed-wing flow control analysis [53] is

$$c_\mu = \frac{\dot{m}_j U_j}{q_\infty S} \tag{8}$$

where $\dot{m}_j$ is the jet mass flow, U_j is the jet speed, q_∞ is the freestream dynamic pressure, and S is the wing planform area. The problem with this approach is that the freestream dynamic pressure is zero during hover, resulting in a numerical singularity. Other researchers have used the fan tip speed as the reference velocity in the blowing momentum coefficient for the ducted-fan application [22]. Although the fan tip speed offers a consistent way to normalize the data, it can

be several times higher than the velocity of the induced flow interacting with the flow control jets. To be more comparable with jet momentum coefficients for other applications, the speed of the flow inside the duct was chosen as a better reference for nondimensional jet analysis. The flow induced through a hovering ducted fan can be calculated from momentum theory as noted in [19] (with no duct contraction or expansion) to be

$$V_{\text{induced}} = \sqrt{\frac{T}{\rho A_{\text{disc}}}} \tag{9}$$

where T is the thrust, and A_{disc} is the area of the fan. The steady momentum coefficient based upon the dynamic pressure of the induced flow then becomes

$$c_\mu = \frac{\dot{m}_j U_j}{q_{\text{duct}} A_{\text{duct}}}, \qquad q_{\text{duct}} = \frac{1}{2}\rho V_{\text{induced}}^2 \tag{10}$$

where A_{duct} is the projected area of the duct (diameter times chord) to be comparable with the planform area of a wing. Also note that substituting Eq. (9) into Eq. (10) shows that the dynamic pressure in the duct is equivalent to one half of the disk loading.

The synthetic jet oscillatory flow requires special treatment in deriving the equivalent blowing momentum coefficient. Farnsworth et al. [44] have used a blowing momentum coefficient based on the total time-averaged momentum of the outstroke, $\bar{I}_j$, defined as

$$\bar{I}_j = \frac{1}{\tau}\rho l_j w_j \int_0^\tau u_j^2(t)\,\mathrm{d}t \tag{11}$$

where τ is the outstroke time (half the overall period), l_j is the slot length, w_j is the slot width, and u_j is the centerline velocity of the jet, as used in the definition for U_0. Multiplying this value by the total number of jets to get the total momentum imparted and dividing by the induced dynamic pressure and area yields a comparable blowing momentum coefficient:

$$c_\mu = \frac{n\bar{I}_j}{q_{\text{duct}} A_{\text{duct}}} \tag{12}$$

The velocity ratio, as defined by Eq. (13) and adapted from [30], is also of interest in flow control applications:

$$V_R = \frac{U_0}{V_{\text{induced}}} \tag{13}$$

It is defined relative to the induced velocity through the duct, as this is the velocity representative of the flow on which the control is acting for this application. For the tests performed, the synthetic jets operated in the range of $V_R = 0.5$ to 1.0, and the steady jets operated in the range of 1.5 to 5.

C. Results and Discussion

Static (hover) tests were performed for both the leading-edge and trailing-edge flow control configurations. Although the concepts were designed to affect the vehicle horizontal flight at high angles of attack, the static capability of these flow control concepts was still of interest. The trailing edge Coandă flow control causes the duct flow to turn and thereby creates normal force. The normal force coefficient data versus jet momentum coefficient are shown in Fig. 19. Data are presented in the form of differences from the base vehicle aerodynamics, since the jet blowing would be used as a control input to affect vehicle flight.

Because the steady blowing was powered by a separate supply of high-pressure air, higher blowing coefficient levels were explored to assess the full capability of the flow control concepts. Figure 19 shows that the synthetic jets were not able to attain the same level of blowing coefficient, but do follow the same trend in force generation. A cubic polynomial curve fit captures the majority of the trend in the steady jet data, and the synthetic jet data exceed this trend by roughly the magnitude of the uncertainty in this measurement (0.01).

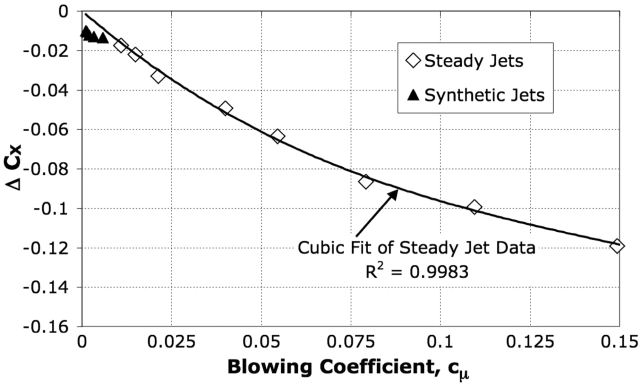

Fig. 19 Static, change in C_X vs blowing coefficient, and trailing-edge flow control.

Therefore, it is likely that synthetic jets are more effective for a given blowing coefficient value, but because of the uncertainty in these data, it is inconclusive.

Figure 20 shows the effect on axial force of the trailing-edge blowing. A positive change in C_Z corresponds to lower thrust. As the flow is expanded by the Coandă blowing, it effectively increases the exit area of the duct and decreases the exit velocity, thereby lowering the net thrust.

Figure 21 shows the effect of trailing-edge blowing on pitching-moment coefficient, the primary objective of the concept. Both steady blowing and synthetic jet blowing produce the intended behavior, with the steady blowing reaching larger values than the synthetic jets due to higher blowing coefficient levels. However, comparing the trends in the data, the synthetic jet effectiveness exceeds the cubic polynomial trend line for steady blowing for a fixed blowing coefficient. The uncertainty for this measurement is 0.004,

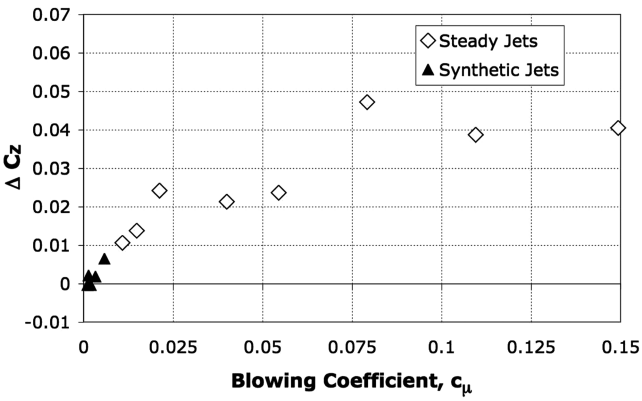

Fig. 20 Static, change in C_Z vs blowing coefficient, and trailing-edge flow control.

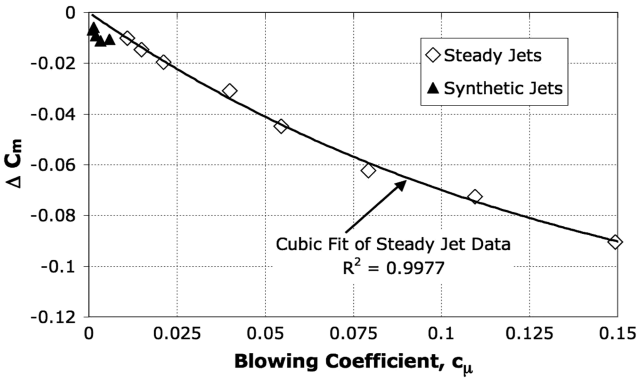

Fig. 21 Static, change in C_m vs blowing coefficient, and trailing-edge flow control.

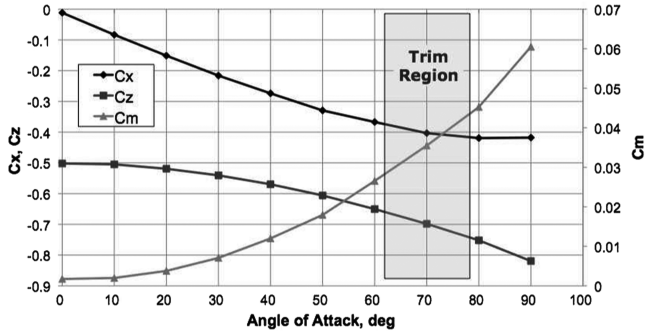

Fig. 22 Baseline vehicle aerodynamic data with trim region.

which cannot account for this difference, thereby supporting the claim that synthetic jets of similar blowing coefficient are more effective.

The leading-edge flow control produced very little effect in static conditions. This is attributed to the duct lip design for smooth and efficient flow in hover. Effectively, the flow is too stable in hover for the synthetic or steady blowing to cause significant separation on the duct lip. However, this does not imply that it will not succeed for its target application of high-angle-of-attack forward flight.

Before discussing the changes in force and moment coefficients due to flow control for flight conditions, it is important to gain a reference point of the underlying vehicle aerodynamics. The baseline vehicle coefficient data for an angle-of-attack sweep at 35 ft/s are shown in Fig. 22.

Figure 22 shows the range of C_X, C_Z, and C_m for the vehicle at a transition speed. The normal force and pitching moment are essentially zero at 0 deg angle of attack (nose directly into the wind) and increase in magnitude as angle of attack increases. The axial force (thrust) is at its lowest magnitude at 0 deg angle of attack (a pure axial climb orientation) and increases as the angle of attack increases. The ducted-fan vehicle tilts into the wind to fly forward, and for this flight speed, it would pitch forward roughly 20 deg. Typically, control vanes in the duct exit flow would be used to counter the nose-up pitching moment to trim the vehicle (attain equilibrium). The 35 ft/s flight speed represents the transition region between hover and high-speed flight that usually requires the highest control vane deflections. Therefore, it is a goal to attain a -0.04 change in pitching-moment coefficient at this flight condition to accomplish vehicle trim solely through flow control actuation. The wind-tunnel test results for 17 and 35 ft/s (10 and 20 kt) are shown in Figs. 23–25.

In Fig. 23, the normal force results show the expected progression in magnitude of the steady results as blowing coefficient increases. The flow control also seems to be slightly more effective at slower flight conditions (17 ft/s), and this would be supported by the fact that the static effects for comparable blowing coefficient were an even larger magnitude ($\sim$0.1). The same trend is observed in the synthetic jets, although the magnitude of the effect is much smaller, due to the lower blowing coefficient.

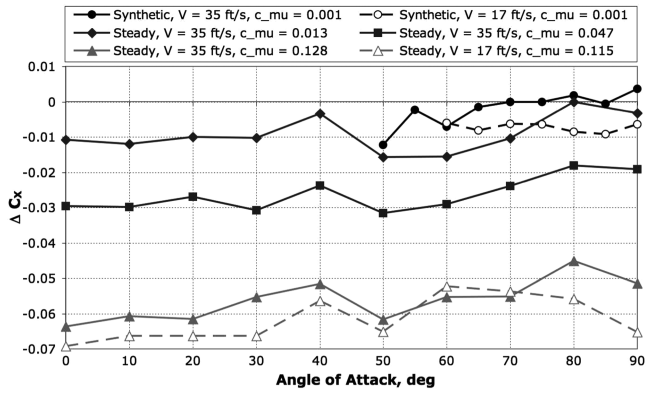

Fig. 23 Forward flight, change in C_X vs angle of attack, and trailing-edge flow control.

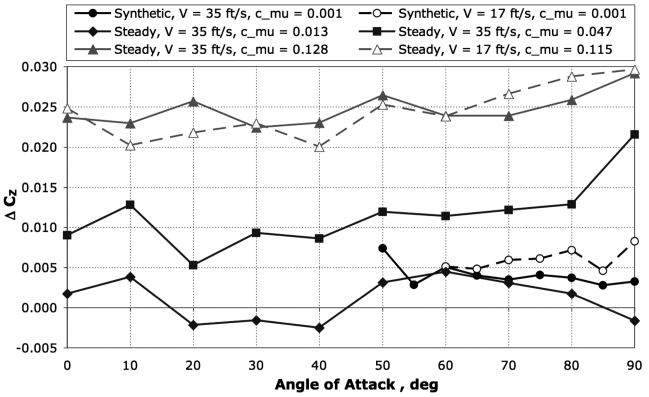

Fig. 24 Forward flight, change in C_Z vs angle of attack, and trailing-edge flow control.

In Fig. 24, the axial force coefficient results show that the flow expansion results in some thrust loss for forward flight, as it did in hover. One aspect to note is that the normal force produced by the flow control is more than double the amount of thrust force lost.

In Fig. 25, the trailing-edge flow control does have a significant effect on vehicle pitching moment. For reference, the value of C_m is on the order of 0.04 for the trim angle of attack of 70 deg at 35 ft/s and 0.035 for a trim angle of attack of 80 deg at 17 ft/s. The highest level of trailing-edge steady blowing can completely cancel that moment for 17 ft/s flight and comes very close for 35 ft/s. It should be noted that this is a very high level of blowing and the synthetic jets are much less effective because of the substantially lower blowing coefficient levels. Again, the steady and synthetic jet flow control is more effective at a lower speed of forward flight, and the steady results show a sudden decrease in effectiveness at high angles of attack (close to trim region). This is due to the fact that the Coandă flow control is trying to turn the ducted-fan flow in the opposite direction to the freestream. As the freestream flow becomes faster, it is more difficult to keep the Coandă flow attached. The conclusion is that the Coandă flow control is more effective at lower angles of attack, where the turned flow is not directly competing with the freestream.

Although the leading-edge flow control showed little effect for the hover condition, it was effective at producing separation on the duct lip for high-angle-of-attack forward flight, as shown in the flow visualization section. The leading-edge concept does not affect normal force, but does produce results in axial force and pitching moment, as shown in Figs. 26 and 27.

Although the trailing-edge flow control concept corresponded to a control moment being created by generating a normal force, the leading-edge concept shows the strong correlation between duct lip thrust and pitching moment. The separation caused on the lip results in thrust loss (Fig. 26) and decrease in pitching moment (Fig. 27). The magnitudes of the changes to pitching moment are roughly half of those seen in the steady trailing-edge flow control, but the

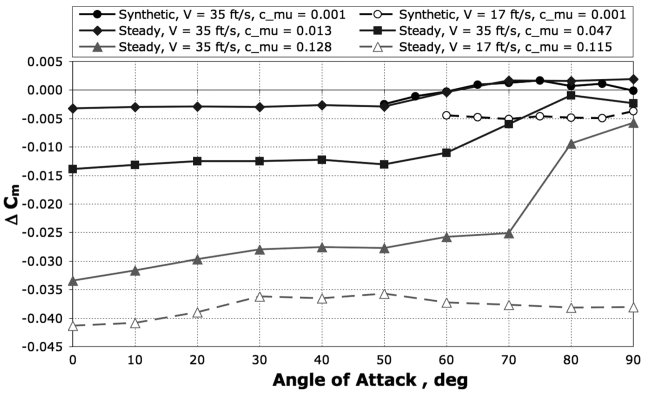

Fig. 25 Forward flight, change in C_m vs angle of attack, and trailing-edge flow control.

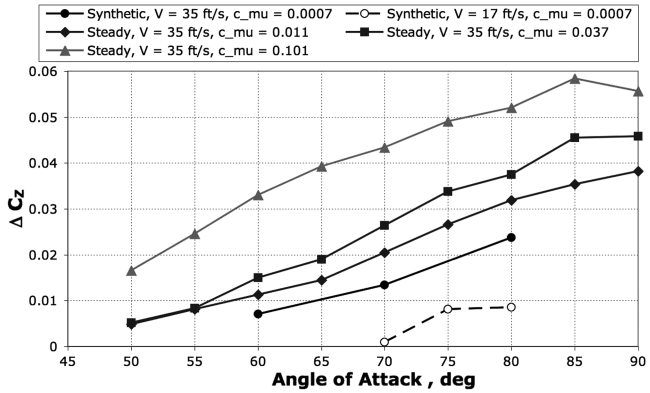

Fig. 26 Forward flight, change in C_Z vs angle of attack, and leading-edge flow control.

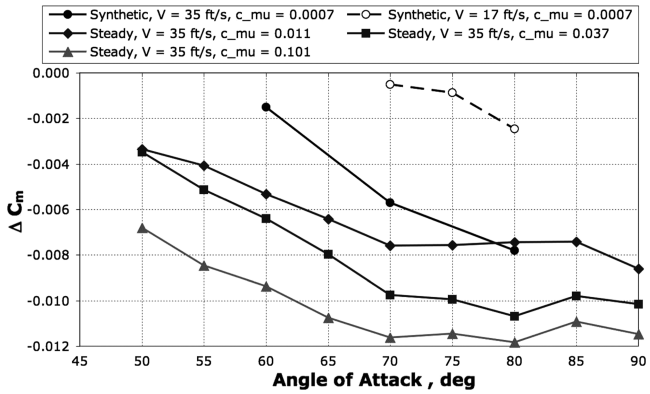

Fig. 27 Forward flight, change in C_m vs angle of attack, and leading-edge flow control.

magnitudes increase with angle of attack, whereas the trailing-edge concept lost effectiveness at these conditions. Higher angles of attack are where the pitching moment is largest, and they represent the area of greatest need for wind-gust rejection. The effects of the leading-edge flow control are smaller than the value needed to completely trim the vehicle, roughly accounting for 25% of the needed −0.04 pitching-moment coefficient to negate the moment. Therefore, an implementation based on this concept could only augment control, but could not be a complete replacement for flight control surfaces.

It should also be noted that the synthetic jets were much more effective in this configuration, but particularly at 35 ft/s, instead of 17 ft/s. Even though the blowing coefficient for the synthetic jets is an order of magnitude lower than the steady blowing, the effects on the overall vehicle forces and moments at 35 ft/s freestream are comparable. This suggests that duct lip separation has more of a digital nature rather than a continuous behavior. In other words, there is a threshold that must be attained to cause separation through actuation, but further increases in actuation power do not return as much benefit. This can also be seen in the steady blowing, where the greatest effect is seen going from no blowing to a blowing coefficient of 0.011. A blowing coefficient 10 times greater only produces about 50% more effect on pitching moment. The lesson to be taken from this is that the nature of the flow one is trying to control is equally important as, or even more important than, the level of blowing being employed. In this particular application of causing separation in a flow that is somewhat unstable, synthetic jets were capable of creating a comparable effect, but at a blowing coefficient that was a fraction of the steady coefficient value.

VII. Conclusions

The new flow control concepts were proven to be successful in producing aerodynamic forces and moments on a ducted fan over a large range of angles of attack through experimental verification. Both synthetic jets and steady jets were capable of modifying the ducted-fan flow, but some cases required high values of steady blowing to create significant responses. Turning of the stream tube exiting the ducted fan was demonstrated using a Coandă surface at the duct trailing edge, thereby creating a normal force and a decrease in pitching moment. Leading-edge separation on the duct lip was induced at high angles of attack through synthetic and steady jet blowing, which also decreased pitching moment. These flow control techniques could be used as control inputs for ducted-fan flight control or augmenting wind-gust rejection performance. The research presented here represents the first time that synthetic jet flow control has been applied to the longitudinal aerodynamics of a ducted-fan configuration.

Attaining high blowing momentum coefficients from synthetic jets is challenging, since the time-averaged velocity is only a function of the outstroke, which equates to the peak velocity divided by π for pure sinusoidal flow. Although peak jet velocities of 225 ft/s (69 m/s) were attained, the synthetic jets operated at lower blowing momentum coefficients than did the steady jets tested. In the trailing-edge flow control cases the ducted-fan application required more authority than the synthetic jets could impart, but this could be overcome with higher-output synthetic jets. In contrast, triggering leading-edge separation on the duct lip was one application in which synthetic jets showed comparable performance with steady jets that were operating at a blowing coefficient that was an order of magnitude higher. These two differing outcomes demonstrate the critical nature of identifying a flow condition that can be sufficiently influenced by the momentum imparted by synthetic jets.

Acknowledgments

The authors would like to thank the U.S. Air Force Research Laboratory for sponsorship of this research through a Phase II Small Business Innovation Research contract and the U.S. Air Force Office of Scientific Research. Thanks also go to colleagues at AVID LLC and the Center for Intelligent Material Systems and Structures of Virginia Polytechnic Institute and State University for their support with experiments and theoretical questions.

References

[1] Smith, B. L., and Swift, G. W., "A Comparison Between Synthetic Jets and Continuous Jets," *Experiments in Fluids*, Vol. 34, 2003, pp. 467-472. doi: 10.1007/s00348-002-0577-6

[2] McMichael, J., Lovas, A., Plostins, P., Sahu, J., Brown, G., and Glezer, A., "Microadaptive Flow Control Applied to a Spinning Projectile," 2nd AIAA Flow Control Conference, AIAA Paper 2004-2512, Portland, OR, 2004.

[3] White, A., "Upgrades for gMAV in Light of Iraq Ops," *UVOnline*, 22 April 2010, http://www.shephard.co.uk/news/uvonline/upgrades-for-gmav-in-light-of-iraq-ops/6185/ [retrieved 12 May 2010].

[4] McCormick, B. W., *Aerodynamics of V/STOL Flight*, Dover, New York, 1999.

[5] Fleming, J., Jones, T., Ng, W., Gelhausen, P., and Enns, D., "Improving Control System Effectiveness for Ducted Fan VTOL UAVS Operating In Crosswinds," 2nd AIAA "Unmanned Unlimited" Systems, Technologies, and Operations, AIAA Paper 2003-6514, San Diego, CA, 15–18 Sept. 2003.

[6] Graf, W., Fleming, J., Ng, W., and Gelhausen, P., "Ducted Fan Aerodynamics in Forward Flight," *AHS International Specialists' Meeting on Unmanned Rotorcraft*, AHS International, Alexandria, VA, Jan. 2005.

[7] Graf, W., "Effects of Duct Lip Shaping and Various Control Devices on the Hover and Forward Flight Performance of Ducted Fan UAVs," Masters Thesis, Virginia Polytechnic Institute and State Univ., Blacksburg, VA, May 2005.

[8] Yaggy, P. F., and Mort, K. W., "Wind-Tunnel Investigation of a 4-Foot-Diameter Ducted Fan Mounted on the Tip of a Semispan Wing," NASA TN D-776, 1961.

[9] Yaggy, P. F., and Goodson, K. W., "Aerodynamics of a Tilting Ducted Fan Configuration," NASA TN D-785, 1961.

[10] Grunwald, K. J., and Goodson, K. W., "Aerodynamic Loads on an Isolated Shrouded-Propeller Configuration for Angles of Attack from −10° to 110 Deg," NASA TN D-995, 1962.

[11] Grunwald, K. J., and Goodson, K. W., "Division of Aerodynamic Loads on a Semispan Tilting-Ducted-Propeller Model in Hovering and

Transition Flight," NASA TN D-1257, 1962.
[12] Mort, K. W., and Yaggy, P. F., "Aerodynamic Characteristics of a 4-Foot-Diameter Ducted Fan Mounted on the Tip of a Semi-Span Wing," NASA TN D-1301, 1962.
[13] Mort, K. W., and Gamse, B., "Wind-Tunnel Investigation of a 7-Foot-Diameter Ducted Propeller," NASA TN D-4142, 1967.
[14] Black, D. M., Wainauski, H. S., and Rohrbach, C., "Shrouded Propellers—A Comprehensive Performance Study," 5th AIAA Annual Meeting and Technical Display, AIAA Paper 1968-994, Philadelphia, Oct. 21–24, 1968.
[15] Martin, P., and Tung, C., "Performance and Flowfield Measurements on a 10-Inch Ducted Rotor VTOL UAV," AHS International, Paper AHS 2004-0264, 2004.
[16] Graf, W., Fleming, J., and Ng, W., "Improving Ducted Fan UAV Aerodynamics in Forward Flight," 46th AIAA Aerospace Sciences Meeting and Exhibit, AIAA Paper 2008-430, Reno, NV, 7–10 Jan. 2008.
[17] Thipyopas, C., Barènes, R., and Moschetta, J., "Aerodynamic Analysis of a Multi-Mission Short-Shrouded Coaxial UAV: part I—Hovering Flight," 26th AIAA Applied Aerodynamics Conference, AIAA Paper 2008-6243, Honolulu, 18–21 Aug. 2008.
[18] Akturk, A., Shavalikul, A., and Camci, C., "PIV Measurements and Computational Study of a 5-Inch Ducted Fan for V/STOL UAV Applications," 47th AIAA Aerospace Sciences Meeting, AIAA Paper 2009-332, Orlando, FL, 5–8 Jan. 2009.
[19] Pereira, J., "Hover and Wind-Tunnel Testing of Shrouded Rotors for Improved Micro Air Vehicle Design," Ph.D. Thesis, Univ. of Maryland, College Park, MD, 2008.
[20] Burley, R., and Hwang, D., "Investigation of Tangential Blowing Applied to a Subsonic V/STOL Inlet," *Journal of Aircraft*, Vol. 20, No. 11, 1983, pp. 926–934.
doi:10.2514/3.48194
[21] Kondor, S., and Heiges, M., "Active Flow Control For Control of Ducted Rotor Systems," *Proceedings, 39th AIAA Aerospace Sciences Meeting & Exhibit*, AIAA Paper 2001-117, Reno, Nevada, Jan. 8–11, 2001.
[22] Kondor, S., Lee, W., Englar, R., and Moore, M., "Experimental Investigation of Circulation Control on a Shrouded Fan," *Proceedings, 33rd Fluid Dynamics Conference*, AIAA Paper 2003-3409, Orlando, FL, June 23–26, 2003.
[23] Kondor, S., "Further Experimental Investigation of Circulation Control Morphing Shrouded Fan," 43rd AIAA Aerospace Sciences Meeting and Exhibit, AIAA Paper 2005-639, Reno, NV, 10–13 Jan. 2005.
[24] Fung, P. H., and Amitay, M., "Control of a Miniducted-Fan Unmanned Aerial Vehicle Using Active Flow Control," *Journal of Aircraft*, Vol. 39, No. 4, 2002, pp. 561–571.
doi:10.2514/2.2993
[25] Fleming, J., Jones, T., Lusardi, J., Gelhausen, P., and Enns, D., "Improved Control of Ducted Fan VTOL UAVs in Crosswind Turbulence," *Proceedings of the 4th AHS Decennial Specialist's Conference on Aeromechanics*, AHS International, Alexandria, VA, Jan. 2004.
[26] Ohanian, O. J., Karni, E., Londenberg, W. K., Gelhausen, P. A., and Inman, D. J., "Ducted-Fan Force and Moment Control via Steady and Synthetic Jets," 27th AIAA Applied Aerodynamics Conference, AIAA Paper 2009-3622, San Antonio, TX, 22–25 June 2009.
[27] Smith, B. L., and Glezer, A., "The Formation and Evolution of Synthetic Jets," *Physics of Fluids*, Vol. 10, No. 9, 1998, pp. 2281–2297.
doi:10.1063/1.869828
[28] Glezer, A., and Amitay, M., "Synthetic Jets," *Annual Review of Fluid Mechanics*, Vol. 34, 2002, pp. 503–529.
doi:10.1146/annurev.fluid.34.090501.094913
[29] Holman, R., Utturkar, Y., Mittal, R., Smith, B. L., and Cattafesta, L., "Formation Criterion for Synthetic Jets," *AIAA Journal*, Vol. 43, No. 10, Oct. 2005, pp. 2110–2116.
doi:10.2514/1.12033
[30] Zhong, S., Jabbal, M., Tang, H., Garcillan, L., Guo, F., Wood, N., and Warsop, C., "Towards the Design of Synthetic Jet Actuators for Full-Scale Flight Conditions, Part 1: The Fluid Mechanics of Synthetic jet Actuators," *Flow, Turbulence and Combustion*, Vol. 78, 2007, pp. 283–307.
doi:10.1007/s10494-006-9064-0
[31] Ramasamy, M., Wilson, J. S., and Martin, P. B., "Interaction of Synthetic Jet with Boundary Layer Using Microscopic Particle Image Velocimetry," *Journal of Aircraft*, Vol. 47, No. 2, 2010, pp. 404–422.
doi:10.2514/1.45794
[32] Gallas, Q., Holman, R., Nashida, T., Carroll, B., Sheplak, M., and Cattafesta, L., "Lumped Element Modeling of Piezoelectric-Driven Synthetic Jet Actuators," *AIAA Journal*, Vol. 41, No. 2, 2003, pp. 240–247.
doi:10.2514/2.1936
[33] Lockerby, D., and Carpenter, P., "Modeling and Design of Microjet Actuators," *AIAA Journal*, Vol. 42, No. 2, 2004, pp. 220–227.
doi:10.2514/1.9091
[34] Sharma, R. N., "Fluid-Dynamics-Based Analytical Model for Synthetic Jet Actuation," *AIAA Journal*, Vol. 45, No. 8, Aug. 2007, pp. 1841–1847.
doi:10.2514/1.25427
[35] Tang, H., Zhong, S., Jabbal, M., Garcillan, L., Guo, F., Wood, N., and Warsop, C., "Towards the Design of Synthetic Jet Actuators for Full-Scale Flight Conditions, Part 1: Low-Dimensional Performance Prediction Models and Actuator Design Method," *Flow, Turbulence and Combustion*, Vol. 78, 2007, pp. 309–329.
doi:10.1007/s10494-006-9061-3
[36] Carpenter, M. H., Singer, B. A., Yamaleev, N., Vatsa, V. N., Viken, S. A., and Atkins, H. L., "The Current Status of Unsteady CFD Approaches for Aerodynamic Flow Control," AIAA Paper 2002-3346, 2002.
[37] Dandois, J., and Garnier, E., "Unsteady Simulation of a Synthetic Jet in a Crossflow," *AIAA Journal*, Vol. 44, No. 2, 2006, pp. 225–238.
doi:10.2514/1.13462
[38] Rumsey, C. L., Schaeffer, N. W., Milanovic, I. M., and Zaman, K. B. M. Q., "Time-Accurate Computations of Isolated Circular Synthetic Jets in Crossflow," *Computers and Fluids*, Vol. 36, 2007, pp. 1092–1105.
doi:10.1016/j.compfluid.2006.09.002
[39] Rumsey, C. L., "Reynolds-Averaged Navier–Stokes Analysis of Zero Efflux Flow Control over a Hump Model," *Journal of Aircraft*, Vol. 44, No. 2, 2007, pp. 444–452.
doi:10.2514/1.23514
[40] Sharma, R. N., and Siong, S. K., "Uniform, Steady Jet, and Synthetic Jet Cross-Flows Across a Circular Cylinder," AIAA Paper 2009-4170, 2009.
[41] Amitay, M., Pitt, D., and Glezer, A., "Separation Control in Duct Flows," *Journal of Aircraft*, Vol. 39, No. 4, 2002, pp. 616–620.
doi:10.2514/2.2973
[42] Gilarranz, J. L., Traub, L. W., and Rediniotis, O. K., "A New Class of Synthetic Jet Actuators—Part II: Application to Flow Separation Control," *Journal of Fluids Engineering*, Vol. 127, 2005, pp. 377–387.
doi:10.1115/1.1882393
[43] Ciuryla, M., Liu, Y., Farnsworth, J., Kwan, C., and Amitay, M., "Flight Control Using Synthetic Jets on a Cessna 182 Model," *Journal of Aircraft*, Vol. 44, No. 2, 2007, pp. 642–653.
doi:10.2514/1.24961
[44] Farnsworth, J. A. N., Vaccaro, J. C., and Amitay, M., "Active Flow Control at Low Angles of Attack: Stingray Unmanned Aerial Vehicle," *AIAA Journal*, Vol. 46, No. 10, Oct. 2008, pp. 2530–2544.
doi:10.2514/1.35860
[45] Vukasinovic, B., Brzozowski, D., and Glezer, A., "Fluidic Control of Separation over a Hemispherical Turret," *AIAA Journal*, Vol. 47, No. 9, 2009, pp. 2212–2222.
doi:10.2514/1.41920
[46] Gomes, L. D., Crowther, W. J., and Wood, N. J., "Towards a Practical Piezoceramic Diaphragm Based Synthetic Jet Actuator for High Subsonic Applications—Effect of Chamber and Orifice Depth on Actuator Peak Velocity," 3rd AIAA Flow Control Conference, AIAA Paper 2006-2859, San Francisco, 5–8 June 2006.
[47] "Assessment of Experimental Uncertainty with Application to Wind Tunnel Testing," AIAA Standard Series, S-071A-1999, AIAA, Reston, VA, 1999.
[48] Barlow, J. B., Rae, W. H., and Pope, A., *Low-Speed Wind Tunnel Testing*, 3rd ed., Wiley, New York, 1999.
[49] Glauert, H., *The Elements of Aerofoil and Airscrew Theory*, 2nd ed., Cambridge Univ. Press, Cambridge, England, U.K., 1983.
[50] Hackett, J. E., Lilley, D. E., and Wilsden, D. J., "Estimation of Tunnel Blockage from Wall Pressure Signatures: A Review and Data Correlation," NASA CR15.224, March 1979.
[51] Mikkelsen, R., and Sørensen, J. N., "Modelling of Wind Tunnel Blockage," *Proceedings of the 2002 Global Windpower Conference and Exhibition* [CD-ROM], European Wind Energy Association, 2002.
[52] Fitzgerald, R. E., "Wind Tunnel Blockage Corrections for Propellers," M.S. Thesis, Univ. of Maryland, College Park, MD, 2007.
[53] Englar, R. J., "Overview of Circulation Control Pneumatic Aerodynamics: Blown Force and Moment Augmentation and Modification as Applied Primarily to Fixed-Wing Aircraft," *Applications of Circulation Control Technology*, AIAA, Reston, VA, 2006, Chap. 2.